Static and time-resolved synchrotron small-angle x-ray scattering studies of lyotropic lipid mesophases, model biomembranes and proteins in solution

2004 J. Phys.: Condens. Matter 16 S327

(http://iopscience.iop.org/0953-8984/16/5/002)

INSTITUTE OF PHYSICS PUBLISHING JOURNAL OF PHYSICS: CONDENSED MATTER

J. Phys.: Condens. Matter **16** (2004) S327–S352 PII: S0953-8984(04)68870-9

Static and time-resolved synchrotron small-angle x-ray scattering studies of lyotropic lipid mesophases, model biomembranes and proteins in solution

Roland Winter and Rudolf Köhling

Department of Chemistry, Physical Chemistry I, University of Dortmund, Otto-Hahn Straße 6, D-44227 Dortmund, Germany

Received 11 September 2003
Published 23 January 2004
Online at stacks.iop.org/JPhysCM/16/S327 (DOI: 10.1088/0953-8984/16/5/002)

Abstract

In this work we discuss the use of small-angle x-ray scattering methods for investigating the temperature and pressure dependent structure and phase behaviour of soft condensed matter and in particular of biomolecular systems, such as lipid mesophases, model biomembrane systems as well as proteins in solution. In addition to temperature, pressure has also been used as a physical parameter in these studies, in particular for studying the energetics and phase behaviour of these systems, but also because high pressure is a feature of certain natural environments and because the high pressure phase behaviour of biomolecules is also of importance for biotechnological applications. By using the pressure jump relaxation technique in combination with time-resolved synchrotron small-angle x-ray scattering, the kinetics of biomolecular phase transitions can be investigated. We applied the technique for studying lipid phase transitions and protein unfolding/refolding reactions. After the discussion of the underlying theoretical concepts, several characteristic examples are presented and discussed.

(Some figures in this article are in colour only in the electronic version)

Abbreviations

SAXS	small-angle x-ray scattering,
TRSAXS	time-resolved small-angle x-ray scattering
MO	monoolein
ME	monoelaidin
LA	lauric acid
DLPC	1,2-dilauroyl-sn-glycero-3-phosphatidylcholine (di-$C_{12:0}$)
DPPC	1,2-dipalmitoyl-sn-glycero-3-phosphatidylcholine (di-$C_{16:0}$)
DOPC	1,2-dioleoyl-sn-glycero-3-phosphatidylcholine (di-$C_{18:1,cis}$)
DOPE	1,2-dioleoyl-sn-glycero-3-phosphatidylethanolamine (di-$C_{18:1,cis}$)
DEPC	1,2-dielaidoyl-sn-glycero-3-phosphatidylcholine (di-$C_{18:1,trans}$)
Snase	staphylococcal nuclease

1. Introduction

The strongest impact of small-angle x-ray scattering (SAXS) in biophysical studies is in the study of structural transitions of biomolecular systems, ranging from gross conformational changes to assembly processes triggered by a variety of perturbations, such as by a biochemical reaction or by a temperature or a pressure jump. The modification of the physico-chemical variables (pH, ionic strength, concentration of reactants, temperature, pressure) can be made gradually through the transition, i.e. the scattering patterns can be recorded at equilibrium at a number of intermediate values. Furthermore, a fast perturbation may be provoked and one follows the relaxation of the system to the new equilibrium state. This requires not only a very intense x-ray beam, available at storage rings, but also instruments for rapid perturbation, such as a fast mixing apparatus (stopped flow) to mix the biomolecule with substrates or to create a pH or ionic strength jump, or a high pressure cell for applying well-defined pressure jumps.

The interest in pressure as a variable has been growing in physico-chemical studies of biological and other soft condensed matter systems in recent years [1–6]. To probe the concept of any energetic description and the resultant set of parameters necessary to provide a general explanation of the phase behaviour of biomolecular systems, one needs to scan the appropriate parameter space experimentally. To this end, pressure dependent studies have also proven to be a very valuable tool. The pressures used to investigate biochemical systems range from 1 to 10 kbar, where the solvent, water, is still in its liquid state at ambient temperatures. Such pressures only change intermolecular distances and affect conformations but do not change covalent bond distances or bond angles. The covalent structure of low molecular weight biomolecules (peptides, lipids, saccharides), like the primary structure of macromolecules (proteins, nucleic acids and polysaccharides), is not perturbed by pressures up to about 20 kbar. Pressure acts predominantly on the spatial (secondary, tertiary, quaternary and supramolecular) structures of macromolecules. Besides the general physico-chemical interest in using high pressure as a tool for understanding the phase behaviour, structure and energetics of biomolecules and amphiphiles in general, high pressure is also of biotechnological (e.g., for high pressure food processing) and physiological (e.g., for understanding the physiology of deep-sea organisms living in cold and high pressure habitats) interest [7–11].

In this work, we first discuss the theoretical background for studying the structure and phase behaviour of lyotropic lipid mesophases (figure 1) and model biomembrane systems using x-ray small-angle scattering techniques. Then we discuss the pressure jump relaxation technique for studying the kinetics of phase transformations between different lipid mesophases. Finally,

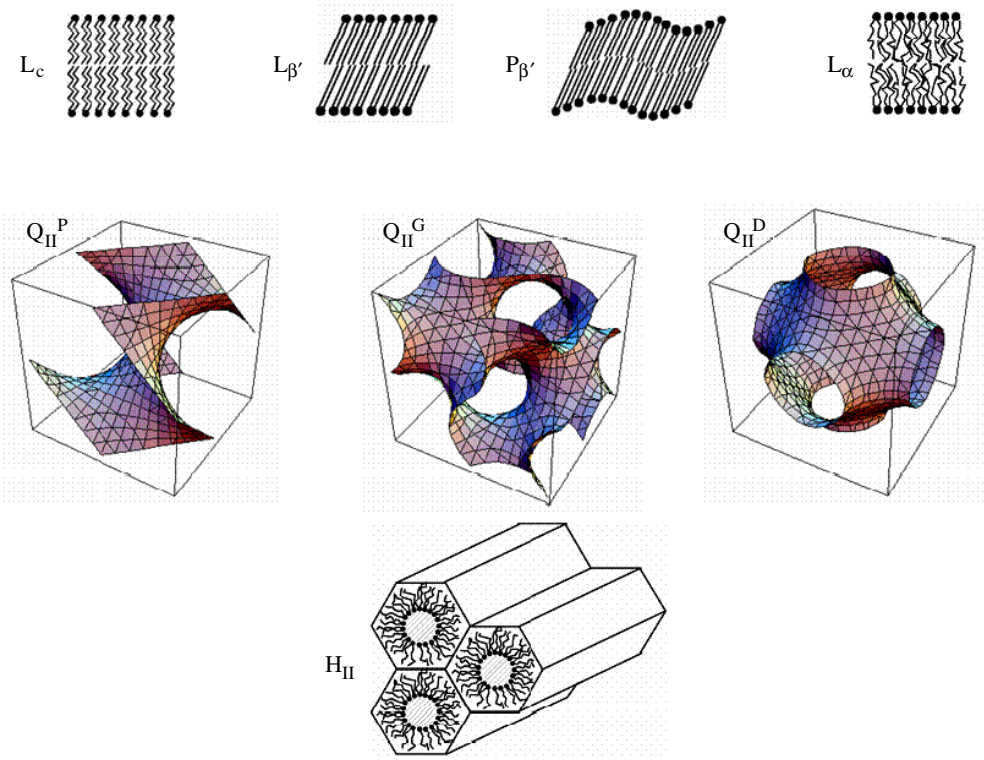

Figure 1. A schematic drawing of lipid–water phases (L_c, lamellar crystalline; $L_{\beta'}$, $P_{\beta'}$, lamellar gel; L_α, lamellar liquid crystalline; Q_{II}^G, Q_{II}^D, Q_{II}^P, inverse bicontinuous cubics; H_{II}, inverse hexagonal). The cubic phases are represented by the G, D and P minimal surfaces, which locate the mid-planes of fluid lipid bilayers.

we illustrate the use of synchrotron x-ray scattering for studying protein structure in solution and unfolding/refolding reactions of proteins. Several representative examples are given.

2. Experimental techniques

The experimental results presented in this work are mainly based on studies using SAXS and wide-angle x-ray scattering (WAXS), partially also in combination with high pressure techniques. The development of synchrotron radiation sources from multi-gigaelectronvolt electron and positron storage rings increased the flux on the sample by factors of more than 10^5 as compared to using conventional laboratory x-ray sources. Use of these sources coupled with efficient electronic detectors made it possible to start collecting SAXS and WAXS data on rapid timescales, which can now go down to tens of milliseconds or even below, thus allowing one to perform also kinetic structural investigations.

For the high pressure x-ray studies, flat diamond cells are generally used. The x-ray pressure cell (figure 2) is home-built and made from stainless steel or a Ni–Cr–Co alloy (NIMONIC 90) of high tensile strength [12, 13]. It has a high pressure connection to the pressurizing system and a bore for a thermocouple. Temperature control is achieved by circulating water from a thermostat through the outside jacket of the vessel. The sample temperature can be controlled within $\pm 0.2\,^\circ$C. For pressures up to 8 kbar, flat diamond

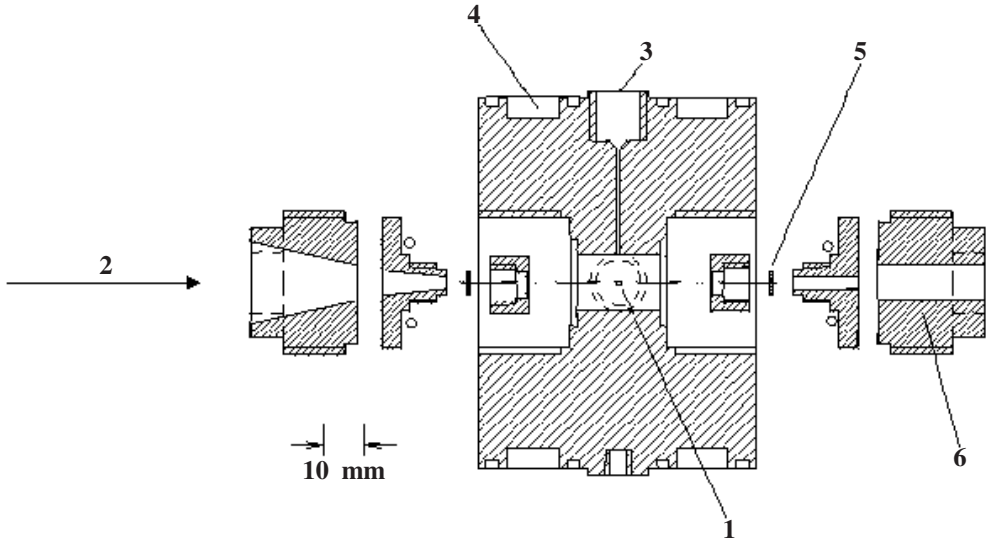

Figure 2. The high pressure sample cell for SAXS studies. The cell is made from NIMONIC 90 alloy with diamond windows (0.8–1 mm thickness) and can be used up to about 8 kbar (1: sample; 2: x-ray beam; 3: high pressure connection; 4: thermostating water circuit; 5: diamond window; 6: closure nut).

windows of 0.8–1 mm thickness are used. The window holders are sealed with Viton-O-rings and are tightened by closure nuts. The sample of 40 μl volume is held in a PTFE ring that is closed with two Mylar foils glued on both sides of the ring to separate the sample from the pressurizing medium (distilled water). The pressurizing system consists of a Heise Bourdon gauge (or an electronic pressure gauge, Sensotec UHP 721-03 or Burster A5-UHP Type 8270) and a hand-operated pressure generator. Pressure jumps are performed by means of a computer-controlled opening of an air-operated valve between the high pressure cell and a liquid reservoir. With this pressure jump apparatus, fast jumps (<5 ms) are possible with variable amplitudes. To minimize adiabatic temperature changes in the course of a kinetic experiment (about 2 mK bar^{-1} under pure adiabatic conditions), the high pressure sample cell was constructed to hold only a very small volume of the pressurizing medium. The pressure jump technique has been shown to offer several advantages over the temperature jump approach:

(1) Pressure propagates rapidly so sample inhomogeneity is a minor problem.
(2) Pressure jumps can be performed bidirectionally, i.e. with increasing or decreasing pressure.
(3) In the case of fully reversible structural changes of the sample, pressure jumps can be repeated with identical amplitudes to allow an averaging of the diffraction data over several jumps and an improvement of the counting statistics.

The static and time-resolved diffraction data presented here have been taken using CCD x-ray detectors (FReLoN or MAR CCD detectors), which consist of a two-dimensional field of 1024 $\times$ 1024 pixels that can be read into a computer (with maximally 14 frames s^{-1}). The faster wire detectors allow shorter acquisition times but, as the acquisition time decreases, the count rate decreases in the same manner. For systems which show intense Bragg scattering, such as lipid mesophases, the exposure time per frame can be as low as 1 ms or even below. For

dilute protein solutions in a high pressure sample environment, the scattering is much weaker so exposure times of the order of 10–100 ms are required [12].

3. Theoretical background

In the following, the basic theoretical concepts for analysing x-ray scattering patterns from partially ordered systems (e.g., membranes, lipid mesophases) and particles (e.g., proteins) in solution are discussed.

3.1. Partially ordered systems: membrane and lipid mesophase diffraction patterns

Biological membranes are the barriers of cells and organelles against the outside medium. They consist of a fluid lipid bilayer with embedded proteins. The amphiphilic character of the lipids with their polar head-group and apolar acyl chains is responsible for the two-dimensional geometry of the lipid matrix. In biophysical studies, lipid bilayer model systems consisting of a few components are generally studied. For investigation of the model biomembrane systems, x-ray (and neutron) diffraction is the most powerful tool for characterizing the topology and packing of the membrane and for following up its changes in environmental conditions, such as ionic strength, temperature and pressure.

Several sample preparation techniques may be used for structural investigations [14–17]. Lipid multi-bilayer films can be prepared and deposited on solid surfaces, such as glass slides, where they adopt a predominant orientation parallel to the bilayer surface. The slide, the level of hydration (relative humidity) of which has to be carefully controlled, is then aligned in an x-ray beam that hits the film tangentially. In the diffraction pattern, equidistant intensity spots on the meridian of the x-ray film exhibit that we have a one-dimensional periodicity along the direction perpendicular to the multilayer film. Off-axis to the equator, reflection spots appear, which originate from the packing of the lipid acyl chains. Instead of films, multilamellar vesicles in solution can be studied. The lipids form onion-like-shaped spherical structures of stacked bilayers with an interlamellar water layer in between. The diffraction pattern then consists of concentric equidistant rings centred around the origin of the diffraction pattern.

In the following, we focus on the solution scattering of multilamellar lipid systems. As regards the diffraction of x-rays, the lipid–water dispersions discussed here are equivalent to powder samples that are composed of many randomly oriented microcrystals. Thus, Bragg's condition is automatically fulfilled and all possible diffraction peaks are simultaneously recorded. While the positions of the diffraction peaks are related to periodic distances within the lyotropic lipid mesophase, their sharpness or width reflects the extent of this periodicity over large distances. The measured reciprocal spacings are given by

$$s = \frac{2}{\lambda} \sin\theta \tag{1}$$

(2θ: scattering angle; λ: wavelength of radiation). If a lipid–water phase is lacking any periodic structure, only diffuse small-angle scattering is observed. Lamellar lipid–water mesophases (denoted as L or P) form alternating layers of lipid and water molecules. This quasi-one-dimensional periodic structure exhibits diffraction patterns in the small-angle regime that are described by the equation

$$s_n = n\frac{1}{d} \tag{2}$$

where $n = 1, 2, 3, \ldots$ and d is the lamellar repeat distance of this one-dimensional lattice, which is the thickness of the lipid bilayer plus that of the adjacent water layer.

Table 1. Miller indices (*hkl*) and the ratio of Bragg peak positions for cubic (Q) and lamellar (L) lipid structures.

$P4_332$ (Q^{212})	$Pm3n$ (Q^{223})	$Pn3m$ (Q^{224})	$Fm3m$ (Q^{225})	$Fd3m$ (Q^{227})	$Im3m$ (Q^{229})	$Ia3d$ (Q^{230})	L	Ratio
							100	1
110	110	110			110			$\sqrt{2}$
111		111	111	111				$\sqrt{3}$
	200	200	200		200		200	2
210	210							$\sqrt{5}$
211	211	211			211	211		$\sqrt{6}$
220	220	220	220	220	220	220		$\sqrt{8}$
221		221					300	3
310	310	310			310			$\sqrt{10}$
311		311	311	311				$\sqrt{11}$
222	222	222	222	222	222			$\sqrt{12}$
320	320							$\sqrt{13}$
321	321	321			321	321		$\sqrt{14}$
400	400	400	400	400	400	400	400	4
410	410	410						$\sqrt{17}$
411	411	411			411			$\sqrt{18}$
331		331	331	331				$\sqrt{19}$
420	420	420	420		420	420		$\sqrt{20}$
421	421	421						$\sqrt{21}$
332		332			332	332		$\sqrt{22}$

Nonlamellar lipid mesophases (figure 1) may also be identified by their characteristic small-angle diffraction pattern. The structure of the inverse hexagonal lipid–water mesophase (denoted as H_{II}) is based on cylindrical water rods, which are surrounded by lipid monolayers. The rods are packed in a two-dimensional hexagonal lattice with Bragg peaks positioned at

$$s = \frac{2}{\sqrt{3}a}\sqrt{h^2 + k^2 + hk}. \tag{3}$$

The lattice constant a is here the distance between the centres of two neighbouring rods and h, k are the Miller indices. The hexagonal lipid phases are easily distinguished from lamellar phases by their ratio of Bragg peak positions, which is $1{:}\sqrt{3}{:}2{:}\ldots$.

Bragg peaks of cubic lipid structures may be observed at

$$s = \frac{1}{a}\sqrt{h^2 + k^2 + l^2} \tag{4}$$

where a is the cubic lattice constant. The Miller indices h, k, l depend on the lattice type (primitive, body centred, face centred) and the symmetry elements of the cubic structure. In table 1 the relative Bragg peak positions of a variety of lipid mesophases including cubic phases are summarized.

The Bragg peaks appearing in addition in the wide-angle region are related to the packing of the lipid acyl chains in a monolayer. Generally, this packing can be described as a centred rectangular lattice with lattice constants a_{rec} and b_{rec}, which are calculated from the observed d-spacings using

$$a_{rec} = 2d_{20} \tag{5}$$

$$b_{rec} = \frac{d_{11}}{\sqrt{1 - [d_{11}/(2d_{20})]^2}}. \tag{6}$$

When the lipid chains are rigidly packed in a hexagonal lattice, only a single wide-angle Bragg peak is usually observed. Then, the lattice constant (chain–chain distance) may be obtained from equation (3). In the case of fluid-like disordered lipid layers, only a very broad wide-angle peak is observed around $s \approx 0.25$ Å^{-1}.

3.2. SAXS studies using solutions of biological macromolecules (in particular proteins)

Generally, the SAXS technique provides us with structural information on inhomogeneities of the electron density with characteristic dimensions between about 10 and 1000 Å. The applications cover fields of all kinds, including alloys, porous media, liquid crystals, polymers, colloids, micelles, microemulsions and biomolecular systems, such as proteins in solution [18–22]. We will focus on the latter class of substances.

The systems that we are interested in have distances that are large compared to interatomic distances. As a consequence, we describe the scattering objects using a continuous function of electron density as determined by the chemical composition of the object. If there are no strong variations of electron density over the molecule (e.g., a native protein), a mean value is assumed. In the case of a more complex and heterogeneous particle, several levels of electron density can be introduced (e.g., RNA in a viral protein capsid). In dilute solution, the scattering objects can be considered to be isolated (intraparticle scattering), whereas in a concentrated solution, the interaction between the particles, displaying spatial correlations, also contributes to the scattering intensity (interparticle scattering).

In the following we discuss the theoretical aspects of SAXS as relevant for dilute systems only [18–25]. We largely follow the nomenclature used by Svergun *et al* [17, 25]. If we place a sample in an x-ray beam, only its electrons will scatter. We consider only elastic scattering processes, i.e., scattering without exchange of energy between the photon and the electron. Let $\rho(\boldsymbol{r})$ be the electron density of the sample at point $\boldsymbol{r}$ and $\boldsymbol{s}_0$ the characteristic wavevector of the incident x-ray beam (with magnitude $|\boldsymbol{s}_0| = 1/\lambda$, where λ is the wavelength of the x-rays). At distances much greater than the size of the sample, the expression for the total scattering amplitude of the scattered x-rays at a point $\boldsymbol{s}$ is

$$F(\boldsymbol{s}) = \int_{V_r} \rho(\boldsymbol{r}) \mathrm{e}^{-2\mathrm{i}\pi \boldsymbol{r}\cdot\boldsymbol{s}} \, \mathrm{d}V_r \tag{7}$$

where $\boldsymbol{s} = \boldsymbol{s}_1 - \boldsymbol{s}_0$ is the scattering vector, $\boldsymbol{s}_1$ is the wavevector of the scattered wave and V_r is the irradiated volume of the sample (particle). The scattering geometry is depicted in figure 3. According to equation (7), $F(\boldsymbol{s})$ is the Fourier transform of the electron density distribution $\rho(\boldsymbol{r})$. If the scattering angle is 2θ, we obtain in the case of elastic scattering, where $|\boldsymbol{s}_0| = |\boldsymbol{s}_1|$, for the modulus of the scattering vector (see figure 3)

$$s = |\boldsymbol{s}| = \frac{2\sin\theta}{\lambda} \simeq \frac{2\theta}{\lambda} \tag{8}$$

for small scattering angles (2θ is generally $<5°$). Sometimes, in particular in the neutron scattering literature, the so-called momentum transfer $\boldsymbol{Q}$ is also used to describe the scattering process, which is $\boldsymbol{Q} = 2\pi\boldsymbol{s}$.

For $\boldsymbol{s} = 0$, we obtain

$$F(0) = \int_{V_r} \rho(\boldsymbol{r}) \, \mathrm{d}V_r = n_\mathrm{e} \tag{9}$$

where n_e is the number of electrons in the volume V_r.

The detector measures the scattered intensity only, which is given by the square of the amplitude resulting from the summation of all the amplitudes of scattered x-rays:

$$I(\boldsymbol{s}) = F(\boldsymbol{s})F^*(\boldsymbol{s}) = |F(\boldsymbol{s})|^2 = \int_{V_r}\int_{V_{r'}} \rho(\boldsymbol{r})\rho(\boldsymbol{r}')\mathrm{e}^{-2\mathrm{i}\pi(\boldsymbol{r}-\boldsymbol{r}')\cdot\boldsymbol{s}} \, \mathrm{d}V_r \, \mathrm{d}V_{r'} \tag{10}$$

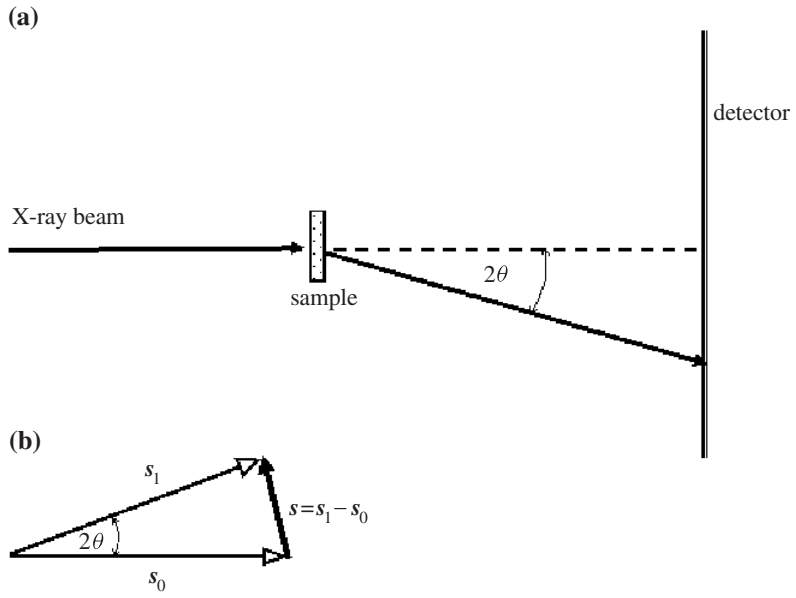

Figure 3. Schematic representations of the scattering process (a) and definition of the scattering vector s.

which involves the separation $\boldsymbol{R} = (\boldsymbol{r} - \boldsymbol{r}')$ of every pair of scattering points and $F^*(\boldsymbol{s})$ is the complex conjugate of $F(\boldsymbol{s})$. (We assume the scattering intensity to be normalized to that of a single electron, taking into account also the polarization factor of the radiation and absorption by the sample.)

The characteristic and pair-distance distribution function. Let $V_r\gamma(\boldsymbol{R})$ be the autocorrelation function of the electron density $\rho(\boldsymbol{r})$ of the sample (particle), defined by

$$\gamma(\boldsymbol{R}) = \frac{1}{V_r}\int_{V_r} \rho(\boldsymbol{r})\rho(\boldsymbol{r}+\boldsymbol{R})\,\mathrm{d}V_r \tag{11}$$

which is called the characteristic function given by Debye and Bueche in 1949; then it follows from equations (10) and (11) that

$$I(\boldsymbol{s}) = \int_V V\gamma(\boldsymbol{R})\mathrm{e}^{-2\mathrm{i}\pi\boldsymbol{R}\cdot\boldsymbol{s}}\,\mathrm{d}V. \tag{12}$$

In the case of particles dissolved in a solvent, the scattering originates from the contrast in electron density between the particle and the surrounding solvent, which is supposed to be homogeneous (having a constant electron density ρ_0). Hence,

$$\Delta\rho(\boldsymbol{r}) = \rho(\boldsymbol{r}) - \rho_0 \qquad \text{and} \qquad F(\boldsymbol{s}) = \int_{V_r} \Delta\rho(\boldsymbol{r})\mathrm{e}^{-2\mathrm{i}\pi\boldsymbol{r}\cdot\boldsymbol{s}}\,\mathrm{d}V_r. \tag{13}$$

Solutions of biological macromolecules, which are essentially composed of light atoms (H, C, N, O, S and P) in water, display rather little contrast of electron density and therefore scatter weakly. This explains the advantage offered by x-ray sources with a very high flux, such as those provided by synchrotron radiation from storage rings.

In the case of solution scattering, the diluted sample is isotropic as the particles take all possible orientations with respect to the direction of the incident beam. Hence, only the

spherical average of the intensity is experimentally accessible, $I(\boldsymbol{s}) = \langle I(\boldsymbol{s})\rangle$, where $\langle\cdots\rangle$ signifies the spherical average. After averaging over all orientations with respect to the beam, using

$$\langle \mathrm{e}^{-\mathrm{i}2\pi \boldsymbol{R}\boldsymbol{s}}\rangle = \frac{\sin(2\pi Rs)}{2\pi Rs} \tag{14}$$

(as given by Debye in 1915), we obtain

$$I(s) = 4\pi \int_0^\infty p(R)\frac{\sin(2\pi Rs)}{2\pi Rs}\,\mathrm{d}R \tag{15}$$

where

$$p(R) = R^2 V\gamma(R) = \frac{1}{\pi}\int_0^\infty RsI(s)\sin(2\pi Rs)\,\mathrm{d}s = \frac{1}{2\pi^2}\int_0^\infty RQI(Q)\sin(QR)\,\mathrm{d}Q. \tag{16}$$

$p(R)$ is called the pair-distance distribution function and is directly connected to the measured scattering intensity. For homogeneous particles, $\rho(\boldsymbol{R}) =$ constant, and $p(R)$ is the histogram of distances between all pairs of points (volume elements) of the particle.

In the following, we assume that we have a monodisperse solution, i.e., all particles are identical. Luckily, this holds true for most biological samples, such as native proteins or viruses. In the case of a solution of a denatured protein, the solution is chemically monodisperse (one molecular species), but polydisperse in shape (the molecules adopt many different disordered conformations). Therefore, there is only one kind of particle in solution with an associated electron density distribution $\rho(\boldsymbol{R})$ and a scattered intensity $I_1(s)$. In sufficiently diluted solution, all particles scatter independently and the resulting intensity scattered by the sample is simply the sum of all the contributions from individual molecules:

$$I(s) = NI_1(s) \tag{17}$$

where N is the number of particles in the sample.

The scattered intensity at $s = 0$ is given by

$$I_1(0) = \int_{V_r}\int_{V_{r'}} \Delta\rho(\boldsymbol{r})\Delta\rho(\boldsymbol{r}')\,\mathrm{d}V_r\,\mathrm{d}V_{r'} = \Delta n_\mathrm{e}^2 \tag{18}$$

where Δn_e is thus the number of excess electrons, i.e. the difference between the number of electrons of the particle and that of the volume of solvent (mostly water or buffer) displaced by the molecule. If the intensity of the incident beam is known on an absolute scale, then the intensity at the (extrapolated) origin ($s = 0$) provides a determination of the molecular mass of the particle, provided that the particle concentration and specific volume as well as the scattering length density of the solvent are known. This requires the absolute scattered intensity and the excess scattering density to be measured with high accuracy, however.

Guinier approximation. If the scattered intensity is expanded in powers of s^2 close to the origin ($s = 0$), the expansion can be restricted to the first terms:

$$I(s) = I(0)\left[1 - \frac{4\pi^2}{3}R_\mathrm{g}^2 s^2 + \cdots\right] \cong I(0)\exp\left(-\frac{4\pi^2}{3}R_\mathrm{g}^2 s^2\right) = I(0)\exp\left(-\frac{1}{3}R_\mathrm{g}^2 Q^2\right). \tag{19}$$

The Guinier approximation replaces the sine expansion with the exponential function. Hence, in the vicinity of the origin, the scattering curve of any isolated particle can be approximated by a Gaussian, the width of which is proportional to the square of the radius of gyration of the particle, R_g, defined by

$$R_\mathrm{g}^2 = \frac{\int_{V_r}\Delta\rho(r)r^2\,\mathrm{d}V_r}{\int_{V_r}\Delta\rho(r)\,\mathrm{d}V_r} \tag{20}$$

where the origin of vectors $\boldsymbol{r}$ is now taken to be the centre of mass of the particle. In practice, a linearized representation will be used to determine R_g, by plotting $\ln[I(s)]$ versus s^2 (Guinier plot). Linear regression yields the radius of gyration from the slope. The validity of the Guinier region is given by the particle's size and shape. In the case of spherical particles, where $R_g = (3/5)^{1/2}R$ (R radius of particle), the Guinier approximation is valid up to $sR_g \approx 0.1$. If several species are present in solution (e.g. oligomers of proteins due to aggregation), their scattering adds up and, in most cases, the value of R_g for the monomer cannot be unambiguously retrieved. Furthermore, the determination of the radius of gyration will be erroneous if the interactions between particles are not negligible. To keep them to a minimum, experiments have to be performed at several concentrations, which should be as low as possible, and then extrapolation to zero concentration is performed.

Global particle scattering. The particle and solvent are assumed to be homogeneous and have constant electron densities. The scattering factor of a particle in dilute solution is then given by its intraparticle form factor $P(\boldsymbol{s}) = F(\boldsymbol{s})F^*(\boldsymbol{s})$, which can be calculated for simple homogeneous triaxial bodies. For a sphere of radius R (e.g. a homogeneous spherical micelle), we obtain

$$\frac{I_1(x)_{\text{sphere}}}{I(0)} = P(x)_{\text{sphere}} = \left[\frac{3(\sin x - x\cos x)}{x^3}\right]^2 \tag{21}$$

where $x = 2\pi sR = QR$, which approaches $P(s) \sim s^{-4}$ at large s values.

Similar equations are given for hollow spheres, cylinders and ellipsoids of revolution as well as for polymer chains [18, 19, 23, 25].

In the case of an unfolded protein, the description in terms of a compact, more or less globular particle is no longer valid, and models developed for polymers may be better suited. A Gaussian chain, the simplest model, is described as a linear association of monomers of constant length with only short range interactions between adjacent units and no correlations between the adjacent segments. The distance between any pair of units at a sufficient distance along the chain follows a Gaussian distribution. Debye established the expression for the scattering intensity of a Gaussian chain:

$$\frac{I_1(s)}{I(0)} = \frac{2(\mathrm{e}^{-x} + x - 1)}{x^2} \tag{22}$$

where $x = (2\pi sR_g)^2$. The scattering intensity thus depends on a single parameter, the radius of gyration R_g. The Guinier approximation still holds for such an expanded structure, but its range of validity is restricted to the immediate vicinity of the origin. At large s, the scattering intensity has the following limit:

$$\lim_{s\to\infty}[s^2I(s)] = \frac{2[1 - \frac{1}{s^2R_g^2}]}{R_g^2}. \tag{23}$$

$I(s)$ varies as s^{-2} instead of showing the s^{-4} behaviour of the Porod law for globular particles. This difference in asymptotic behaviour provides a way of monitoring the degree of folding of a protein upon denaturation induced by temperature, pressure, pH or a denaturing agent. It is most conveniently represented using the so-called Kratky plot of $s^2I(s)$ versus s. The scattering curve of a globular particle will exhibit a distinctive bell-shaped curve with a maximum, the position of which depends on the radius of gyration, while a Gaussian chain shows a plateau at larger s values. Real chains have longer extensions due to the stiffness of bonds and intrachain interactions (excluded volume effect). Approximate expressions for their scattering curves are available for such chains as well (e.g. [18, 25] and references therein).

Porod invariant. The autocorrelation function, as given by equation (16), at $R = 0$, is

$$V\gamma(0) = 2\int_0^\infty s^2 I(s)\,\mathrm{d}s \tag{24}$$

while, from the definition of $\gamma(R)$, we obtain

$$\gamma(0) = \frac{1}{V}\int_{V_r} \Delta\rho(\boldsymbol{r})\Delta\rho(\boldsymbol{r})\,\mathrm{d}V_r = \overline{\Delta\rho^2} \tag{25}$$

so

$$V\gamma(0) = V\overline{\Delta\rho^2} = \tilde{Q}. \tag{26}$$

Hence, integrating $s^2 I(s)$ twice over the whole reciprocal space s yields an invariant, $\tilde{Q}$, the so-called Porod invariant. It is related to the mean square contrast of the electron density of the particle, $\overline{\Delta\rho^2}$, irrespective of its structure.

Hydrated volume. The x-ray scattering pattern contains information not only on the size and shape of the particles, but also on their interactions within the solvent. Hence, one is able to measure the hydrated volume of the particle. The intensity $I_1(0)$ scattered at the origin by a particle (equation (18)) can be written as

$$I_1(0) = (V\overline{\Delta\rho})^2 \tag{27}$$

where V is the volume of the hydrated particle. If the particle has a homogeneous density, $(\overline{\Delta\rho})^2 = \overline{\Delta\rho^2}$, we obtain for the hydrated volume of the particle

$$V = \sqrt{\frac{I_1(0)}{\gamma(0)}} = \frac{I_1(0)}{\tilde{Q}}. \tag{28}$$

The asymptotic regime. If the particle has a uniform electron density distribution and a sharp interface with the solvent, Porod showed that the asymptotic behaviour of the scattered intensity is given by

$$8\pi^3 \lim_{s\to\infty}[s^4 I_1(s)] = A_s\overline{\Delta\rho^2} + Cs^4 \tag{29}$$

where A_s is the area of the interface between the solute and the solvent and C is a correction term, taking into account the existence of short distance density fluctuations as well as experimental uncertainties of the scattering intensity at large angles.

Data processing. The main task of the data processing is to restore the scattering intensity $I(s)$ from the experimental data set $I_{\exp}(s)$. For monodisperse systems, $I(s)$ is related to the pair-distance distribution function of the particle $p(r)$ by the Fourier transform

$$I(s) = 4\pi\int_0^{D_{\max}} p(r)\frac{\sin(2\pi sr)}{2\pi sr}\,\mathrm{d}r \tag{30}$$

where $D_{\max}$ is the maximum diameter of the particle. This is equation (15), but the upper bound of the integral is now $D_{\max}$. The function $p(r)$ measures the distribution of pairwise distances within the volume of the scattering particle, or, in other words, is the density contrast pair correlation function of the molecule. The function $p(r)$ contains the same information as $I(s)$ and the data processing can be done 'indirectly' by restoring the $p(r)$. In this 'indirect Fourier transform' approach, which was first introduced by Glatter [19], $p(r)$ is expressed as a linear combination of spline functions, as a Fourier series or as Hermite polynomials [18, 25–27] and this method is superior to other data processing techniques.

The radius of gyration is derived from $p(r)$ through the relationship

$$R_g^2 = \frac{\int r^2 p(r)\,dr}{2\int p(r)\,dr}. \tag{31}$$

This expression, making use of the whole measured scattering curve, is much less sensitive to factors such as the presence of residual interparticle interactions or a small amount of aggregates than the computationally more straightforward Guinier relation.

In keeping with the low resolution of the solution scattering studies, the data interpretation is usually performed in terms of homogeneous bodies. The standard trial-and-error approach involves the evaluation of the scattering patterns from different models and their comparison with the experimental data. The reliability and/or resolution of the shape restoration can be enhanced if information about the particle is available. A necessary prerequisite is the accurate evaluation of scattering patterns from atomic models taking into account the influence of the solvent. Several helpful programs are available today. The program CRYSOL [26] calculates the x-ray scattering curves from atomic models (e.g. the crystal structure from a PDB file) taking into account also the scattering from a ∼3 Å solvation shell (interestingly, the scattering density of water in the border layer of proteins is on average typically 1.05–1.25 times that of the bulk, which is due to a higher density of the bound solvent). The program DAMMIN restores the *ab initio* low resolution shape and internal structure of biological macromolecules in solution from isotropic scattering, using a multiphase model of the particle built from densely packed dummy atoms and simulated annealing is employed to find a configuration that fits the data minimizing the interfacial area [25, 27, 28].

4. Examples

4.1. Lipid bilayers and nonlamellar lipid phases

Lyotropic lipid mesophases are organized molecular systems formed by amphiphilic molecules, such as phospholipids, in the presence of water. They exhibit a rich structural polymorphism, depending on their molecular structure and environmental conditions, such as water content, pH, ionic strength, temperature and pressure [29–33]. The basic structural element of biological membranes consists of a lamellar phospholipid bilayer matrix. In the lamellar structure, the interfaces are flat and are periodically stacked forming multilamellar vesicles. Two neighbouring lipid bilayers are separated by a water layer of about 10–20 Å.

Saturated phospholipids often exhibit two thermotropic lamellar phase transitions, a gel to gel ($L_{\beta'}/P_{\beta'}$) pretransition and a gel to liquid crystal ($P_{\beta'}/L_\alpha$) main transition at a higher temperature T_m (for the structures, see figure 1). In the fluid-like L_α phase, the acyl chains of the lipid bilayers are conformationally disordered (they contain more gauche conformations that result from rotations around C–C bonds by +120° or −120°), whereas in the gel phases, the chains are more extended and ordered. Because the average end-to-end distance of disordered hydrocarbon chains in the L_α phase is smaller than that of ordered (all-*trans*) chains, the bilayer becomes thinner during melting at the $P_{\beta'}/L_\alpha$ transition, even though the lipid volume increases by about 3% [34]. In addition to these thermotropic phase transitions, pressure induced phase transformations have been observed ([13] and references therein). Upon compression, the lipids easily adopt to volume restriction by changing their conformation and packing. Lipid systems are these biological systems which are most pressure sensitive and in general they easily undergo phase transformations under changes of environmental conditions.

As an example, figure 4(a) shows small-angle diffraction data for a DPPC bilayer in excess water as a function of temperature. Clearly the pretransition as well as the main lipid phase

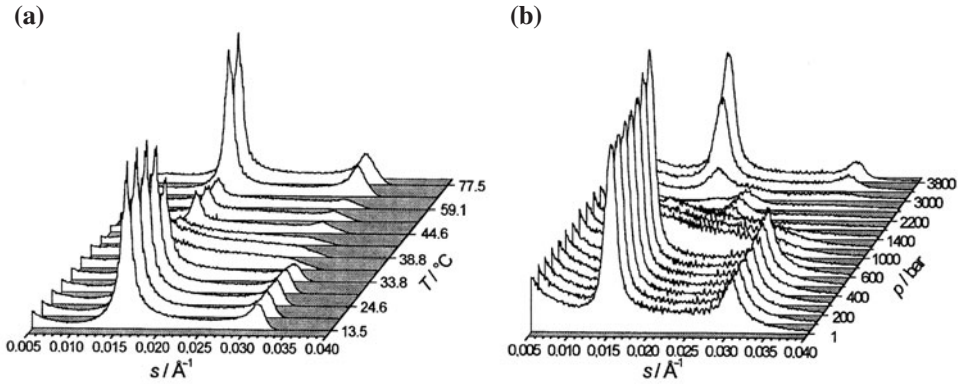

Figure 4. Typical temperature (a) and pressure (b) dependent (at $T = 55\,^{\circ}\mathrm{C}$) small-angle x-ray scattering patterns of DPPC bilayers in excess water. Only one or two orders of lamellar Bragg reflections are visible.

transition are observed as relatively sharp shifts of the Bragg peak positions at about 35 and 42 °C, respectively. The lamellar lattice constant increases from ∼63 Å in the $L_{\beta'}$ phase to ∼72 Å in the ripple gel phase $P_{\beta'}$. In the fluid L_α phase, the Bragg peaks are further apart, which means that the bilayer plus water layer becomes smaller. This is a result of a reduction in the thickness of the lipid acyl chains due to segmental disorder. Because of the highly disordered chains in the fluid L_α phase, the bilayer thickness decreases to a lattice constant of about 66 Å. Figure 4(b) shows some pressure dependent data. In DPPC dispersions at 55 °C, a shift to lower scattering vectors together with a change in the lineshape is observed at 800 bar which is due to the pressure induced L_α to $P_{\beta'}$ phase transition; the corresponding lattice constant increases from 68 to 71 Å. Further increase in pressure leads to the formation of a pressure induced interdigitated gel phase, $L_{\beta\mathrm{i}}$, around 1400 bar, where the lipid acyl chains from opposing monolayers partially interpenetrate, which leads to a decrease of the lamellar repeat period to about 50 Å. At ∼2.8 kbar, the transition to the gel 3 phase occurs at this temperature with a lattice constant that is about 10 Å larger [35, 36].

We note that applying high pressure can lead to the formation of additional gel phases, which are not observed under ambient pressure conditions, such as the interdigitated high pressure gel phase $L_{\beta\mathrm{i}}$ found for phospholipid bilayers with acyl chain lengths $\geqslant$C16 [36, 37]. To illustrate this phase variety, the results of a detailed x-ray diffraction and FT-IR spectroscopy study of the p, T phase diagram of DPPC in excess water are shown in figure 5 [36]. The structures of the L_α, $P_{\beta'}$ (gel 1), $L_{\beta'}$ (gel 2), gel 3, gel 4 and gel 5 phases are illustrated schematically in figures 1 and 5. In the gel 5 phase the lipid molecules have lost essentially all the interlamellar hydrating water, which now coexists as bulk frozen water (ice VI).

It is now well known that many biological lipid molecules also form nonlamellar liquid crystalline phases (see figure 1) [31–33, 39]. Lipids, which can adopt a hexagonal phase, are present at substantial levels in biological membranes, usually with at least 30 mol% of the total lipids. It is generally assumed that the nonlamellar lipid structures, such as the inverted hexagonal (H_{II}) and cubic (Q_{II}) lipid phases, are also of biological relevance. Fundamental cell processes, such as endocytosis and exocytosis, fat digestion, membrane budding and fusion, involve a rearrangement of biological membranes where nonlamellar lipid structures are probably involved. Also static cubic structures (cubic membranes) might occur in biological cells [33, 38, 39]. Recently, cubic lipid phases became also of interest for crystallizing membrane proteins [33]. The structures of the most common cubic phases, $Q_{\mathrm{II}}^{\mathrm{G}}$,

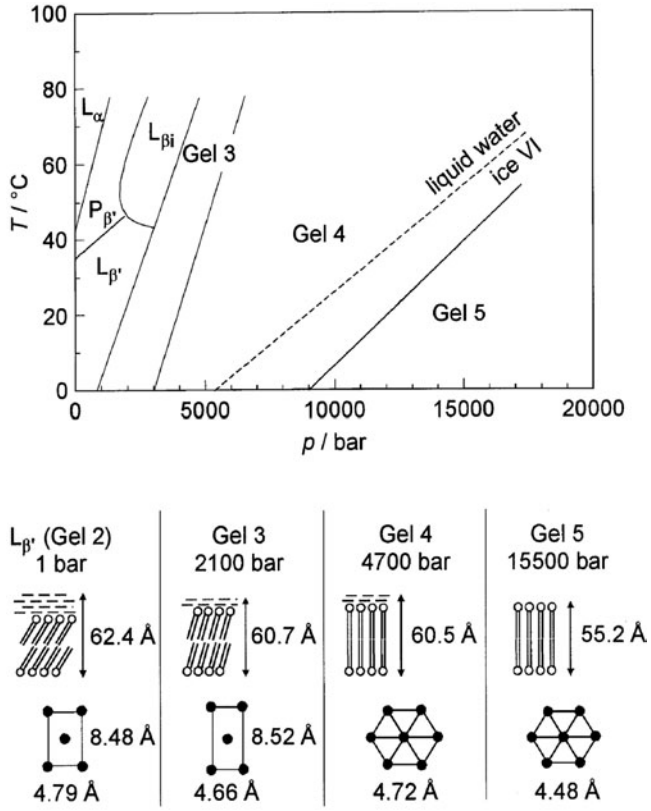

Figure 5. The T, p phase diagram of DPPC bilayers in excess water and a schematic drawing of the lamellar lattice constant and lipid packing in the bilayer plane of DPPC gel phases at 23 °C. It is noteworthy that an additional crystalline gel phase (L_c) can be induced in the low temperature regime after prolonged cooling.

Q_{II}^{D} and Q_{II}^{P}, are closely related to the Schoen gyroid (G), the Schwarz D and the Schwarz P infinite periodic minimal surfaces (IPMS). An IPMS is an intersection-free surface periodic in three dimensions with a mean curvature that is everywhere zero. Draping a lipid bilayer onto these IMPS leads to three lipid inverse cubic phases of crystallographic space groups $Im3m$ (P), $Pn3m$ (D) and $Ia3d$ (G), respectively (figure 1). The surfaces are related to each other by a Bonnet transformation, which is a one-to-one isometric mapping between identical surface patches. The surface that sits at the lipid bilayer mid-plane separates two interpenetrating but not connected water networks.

We will discuss lipid–water systems with the lipids taken from different types of amphiphilic molecule. In contrast to DOPC, which shows a lamellar L_β–L_α transition only, the corresponding lipid DOPE with the smaller head-group ethanolamine exhibits an additional phase transition from the lamellar L_α to the nonlamellar inverse hexagonal H_{II} phase, when it is dispersed in water. As pressure forces a closer packing of the lipid chains, which results in a decreased number of gauche bonds and kinks in the chains, both transition temperatures, of the L_β–L_α and the L_α–H_{II} transitions, increase with increasing pressure. In figure 6, the T, p phase diagram of DOPE in excess water is displayed. The slope of the L_α–H_{II} transition is almost three times larger than that of the L_β–L_α transition; values of about 40 and 14 °C kbar^{-1}

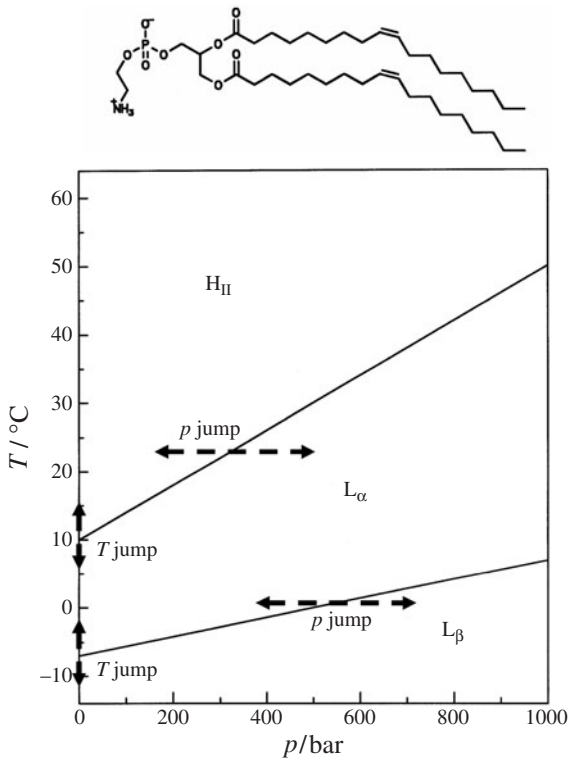

Figure 6. The T, p phase diagram of DOPE (molecular structure at the top) in excess water. The dashed arrows indicate how by using fast T or p jumps the kinetics of the different phase transformations could be studied.

have been found, respectively. The reason that the former transition has such a strong pressure dependence could be conjectured to be the strong pressure dependence of the chain length and volume of its unsaturated chains.

Finally, one further example of single-component lyotropic lipid systems exhibiting nonlamellar phases is discussed: ME and MO dispersed in excess water. Their hydrocarbon chain which contains one double bond, at the ninth carbon atom, is attached to the first carbon atom of glycerol. ME and MO differ only in the configuration of the double bond in their single acyl chain, which is *trans* in ME and *cis* in MO. In contrast to the preceding example, ME and MO form spontaneously cubic phases over wide ranges of temperature and hydration [40–43]. The T, p phase diagrams of ME and MO in excess water are presented in figure 7, in addition to some characteristic diffraction patterns for MO. As can clearly be seen, the small change in the acyl chain double-bond configuration, from *trans* (ME) to *cis* (MO), causes a dramatic change in the observed phase behaviour. In the system MO–water, the cubic Q_{II}^{D} phase is stable over wide ranges of temperature and pressure. The *cis* configuration of MO leads to a more wedge-like molecular shape and a strong tendency for a MO monolayer to curve toward the water. Hence, the formation of lamellar phases, which requires a cylindrical molecular shape, is disfavoured.

Not only the nature of phospholipid phase transitions, but also the way in which they are affected by the incorporation of other species interacting with these membranes has attracted considerable experimental and theoretical attention. Firstly, they intimately reflect the

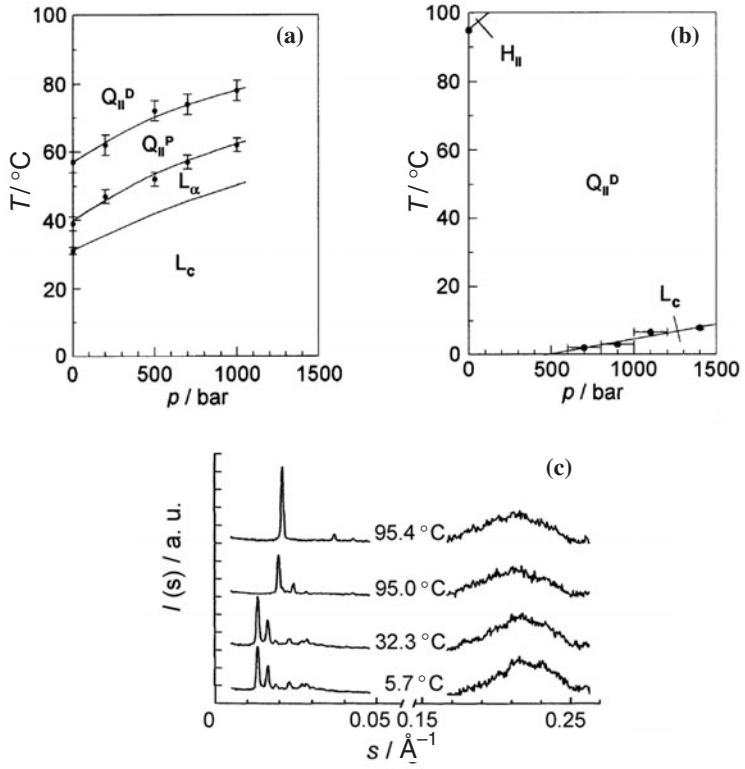

Figure 7. The T, p phase diagram of (a) ME and (b) MO in excess water. (c) As typical examples for diffraction patterns, the small- and wide-angle scattering intensity of a 20 wt% MO–H_2O dispersion is shown at selected temperatures. At low temperature, the (110), (111), (200), (211), (220) and (221) reflections of the cubic $Pn3m$ phase are visible. At about 95 °C, reflections which are spaced in the ratio 1:$(3)^{1/2}$:2, corresponding to the (10), (11) and (20) reflections of the H_{II} structure, appear. The broad wide-angle scattering peak reflects the disordered packing of the acyl chain, which is typical for the fluid-like chain in both of these lipid phases.

molecular interactions of the membrane and may thus help in understanding membrane systems and function on a molecular level. Secondly, the addition of steroids, peptides, anaesthetics and drugs to membrane systems is of biological and pharmacological relevance. Generally, changes in lipid conformation, phase separation or transitions to other lamellar or to nonlamellar phases can be observed upon incorporation of additives into lipid bilayer membranes. For typical examples, see [29, 30, 13, 44–48].

4.2. Kinetics of phase transformations in lipid systems

Phase transitions between lipid mesophases must be associated with deformations of the interfaces which, very often, imply also their fragmentation and fusion with the result that not only does the topology change, but so also does the symmetry of the lipid aggregate. Depending on the topology of the structures involved, transition phenomena of different complexity are observed. In addition, the transition rates and mechanisms depend on the level of hydration of the structures involved and on the forces driving the transition. We used the synchrotron x-ray diffraction technique to record the temporal evolution of the structural changes after induction of the phase transition by a fast jump across the phase boundaries [49, 50]. As

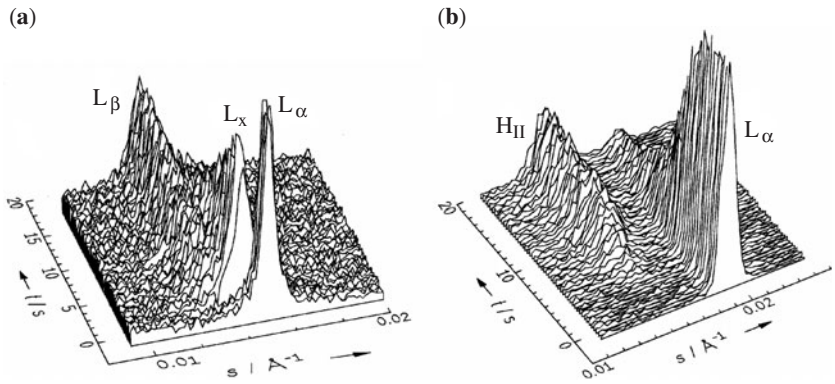

Figure 8. Diffraction patterns of (a) DEPC in excess water after a pressure jump from 200 to 370 bar at 18 °C and (b) DOPE in excess water after a pressure jump from 300 to 110 bar at 20 °C.

indicated in figure 6, principally, temperature (by fast laser heating [51]) or pressure jumps can be used to trigger the lipid phase transitions [49–55]. We have used pressure jump techniques in conjunction with synchrotron x-ray diffraction to study the time course of lipid phase transitions and to search for possible transient intermediate structures, with a view to unravelling the underlying transition mechanisms. We discuss two representative examples.

Experiments for investigating the lamellar–H_{II} transition kinetics have been performed, for example, on DOPE dispersions. The T, p phase diagram of DOPE in excess water is depicted in figure 6. Figure 8 shows the diffraction patterns of DOPE at 20 °C after a pressure jump from 300 to 110 bar. Clearly, the (001) reflection of the L_α phase and the (10) reflection of the developing H_{II} phase can be identified. In this case, a two-state mechanism is observed. Interestingly, we find that successive pressure jumps lead to an acceleration of the phase transition kinetics. The half-transit time decays from 8.5 s for the first pressure jump to 5.3 s after the fourth jump. After the pressure jump, an induction period of several seconds is observed before the first Bragg reflections of the newly formed H_{II} phase appear. Upon successive pressure cycles, this induction period decreases. An explanation for this phenomenon might be the formation of defect structures, such as inverted intermicellar intermediates, which are formed during the pressure cycles and which have not healed between successive pressure cycles. This observation also shows that the history of sample preparation plays an essential role in lipid systems. Figure 9 exhibits the time course of lattice constants and half-widths of the Bragg reflections of the L_α and H_{II} phase after the pressure jump. After 20 ms the lattice constant of the L_α phase has slightly decreased, due to fast conformational changes of the lipid molecules. After 250 ms, the lattice constant of the L_α phase, $a(L_\alpha)$, decreases slowly to 50.6 Å. Following an induction period, the Bragg reflection of the H_{II} phase appears; $a(H_{II})$ first decreases slightly and then increases again owing to water uptake by 0.5 up to 73.9 Å within about 30 s. At the same time as the H_{II} phase is formed, $a(L_\alpha)$ decreases rapidly. The decrease in half-width of the (10) reflection of the H_{II} phase with time might be due to an elongation and more efficient packing of the micellar tubes forming the hexagonal structure. As the fully hydrated H_{II} phase needs more water than the lamellar phase and the lattice constant $a(H_{II})$ does not change significantly with time, one can assume that the necessary water uptake occurs within the defect structures being formed during the induction period. These transient structures do not lead to coherent scattering patterns, however.

As an example of an interlamellar phase transformation, we present pressure jump experiments carried out in DEPC–water dispersions to study the L_β–L_α gel to fluid main

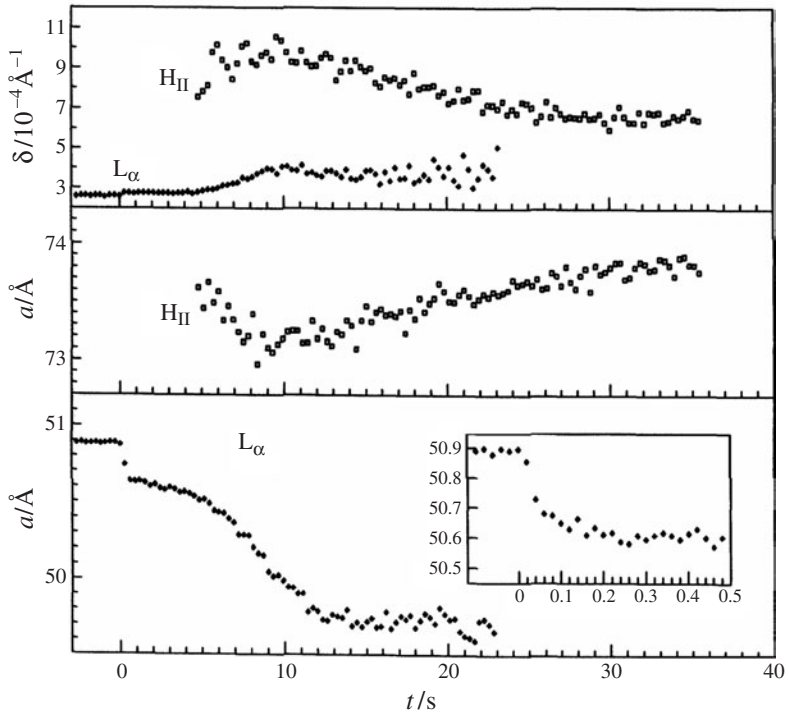

Figure 9. Lattice constants a and half-widths δ of the first-order Bragg reflections of the L_α phase and the H_{II} phase of DOPE in excess water after a pressure jump from 300 to 110 bar at 20 °C.

transition, which occurs at $T_m = 12\,^\circ$C at ambient pressure and which has a pressure dependence of $dT_m/dp = 20\,^\circ$C kbar^{-1}. Selected SAXS diffraction patterns at 18 °C after a pressure jump from 200 bar (L_α phase) to 370 bar (L_β phase) are depicted in figure 8. An intermediate structure is clearly observable in this case. The first-order (001) Bragg reflection of the initial L_α phase ($a = 66$ Å) vanishes in the course of the pressure jump (<5 ms). The first diffraction pattern collected after the pressure jump exhibits a Bragg reflection of a new lamellar structure L_x with a slightly larger d value, which increases with time. The lattice constant of the L_β phase formed is 78 Å. The transition is complete after about 15 s. In equilibrium measurements, no such intermediate lamellar structure is detectable.

Generally, as has been found in studies of pressure and temperature jump induced phase transitions of other systems [49–55], the results show that the relaxation behaviour and the kinetics of pressure induced lipid phase transformations depend drastically on the topology of the lipid mesophase and also on the temperature and the driving force, i.e., the applied pressure jump amplitude, Δp. Often multicomponent kinetic behaviour is observed, with short relaxation times (probably on the nanoseconds to microseconds timescale) in a burst phase relating to the relaxation of the lipid acyl chain conformation in response to the pressure change, which leads to the small changes in the observed lattice constants right after the pressure jumps. The longer relaxation times measured here are due to the kinetic trapping of the system. In most cases, the rate of the transition is limited by the transport and redistribution of water into and in the new lipid phase, rather than being controlled by the time required for a rearrangement of the lipid molecules. The obstruction factor for the different structures controls the different kinetic components. In addition, nucleation phenomena and domain

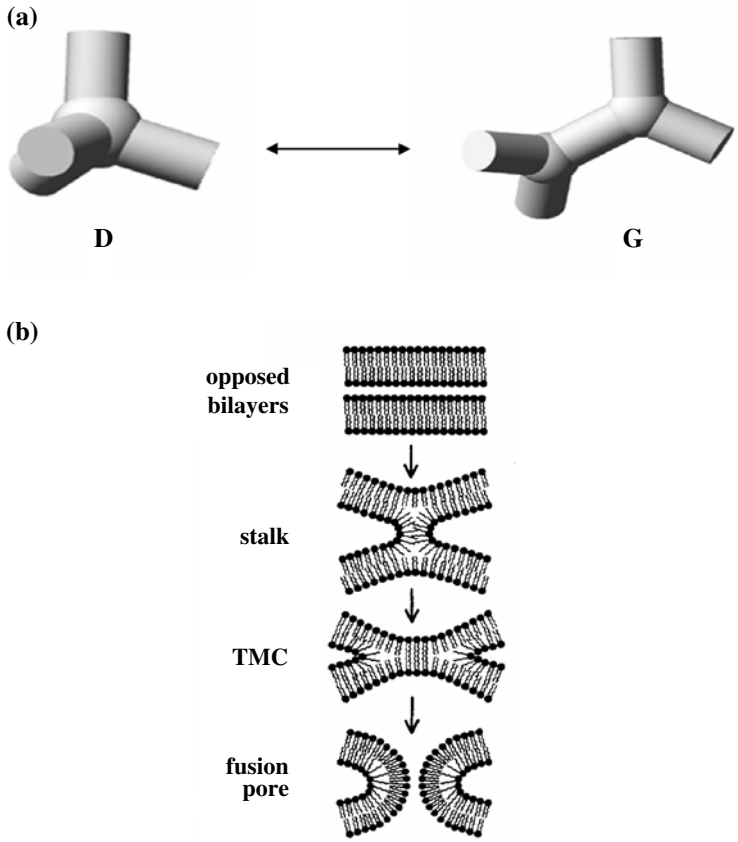

Figure 10. (a) A schematic illustration of the 'stretching' of water channel junctions during the continuous transformation between the D and G cubic phases, which occur with no disruption of the bilayer topology. A junction of four water channels in the Q_{II}^{D} phase is converted into two three-way junctions in the Q_{II}^{G} phase. (b) A possible mechanism of membrane fusion: the monolayers of two opposed lipid bilayers mix to form a stalk intermediate that expands radially to a *trans* monolayer contact (TMC), leading to rupture as a result of curvature and interstitial stresses and finally to the formation of a fusion pore.

size growth of the structures evolving play a role. Also, in particular cases a digression of the mechanism of phase transformation observed under slow scanning equilibrium conditions appears under high free energy gradients (here large pressure jump amplitudes) and the high driving force may drive the system through a correlated ordered intermediate state.

In cases where the transition occurs without change in water content within the mesophase, such as in the intercubic $Q_{II}^{G} \rightarrow Q_{II}^{D}$ transition of the system DLPC-LA (1:2) at a fixed water composition, the kinetics may be much faster [53]. As a mechanism for this cubic–cubic transformation, a stretching mechanism has been proposed whereby each fourfold junction in the Q_{II}^{D} phase is formed by bringing together two threefold junctions in the Q_{II}^{G} phase (figure 10(a)). Recently, it has been suggested that such continuous cubic transitions could also involve noncubic (tetragonal, rhombohedral) distortions of the underlying minimal surfaces, yet with the surfaces remaining minimal during the processes (see [55] and references therein). The inverse bicontinuous cubic phases are of particular relevance to the mechanism

of membrane fusion, which is a ubiquitous process in cell membranes. The reason for this is that the fusion channel between bilayers is closely similar to the local structure of these cubic phases. Indeed, lamellar to cubic phase transitions in lyotropic liquid crystals must occur by a series of fusion events and the bicontinuous cubic phase structures may be viewed as 3D lattices of such fusion pores [54, 55]. Figure 10(b) displays schematically the formation of a fusion pore via a stalk intermediate, which might also play a role in the final step of biological membrane fusion, which uses a variety of fusion proteins for approach and bending of the lipid bilayers.

4.3. Pressure effects on proteins in solution

It has long been known that the application of high hydrostatic pressure results in the disruption of the native protein structure due to the decrease in the volume of the protein–solvent system upon unfolding [56–58]. Pressure denaturation studies thus provide a fundamental thermodynamic parameter for protein unfolding, the volume change ΔV_u°, in addition to an alternative method for perturbing the folded state and thus extracting its stability. A number of reviews on effects of pressure on proteins discuss these volume changes in greater detail [3–6]. Denaturation is usually studied at atmospheric pressure using high temperature guanidinium hydrochloride or urea as denaturants. However, interpretation of the results obtained using such methods may be complicated by the facts that:

(1) varying the temperature changes both the volume and the thermal energy of the system at the same time and
(2) the thermodynamic parameters of denaturation by guanidinium hydrochloride or urea are influenced by the binding of these molecules to proteins.

By contrast, if denaturation is induced at constant temperature in the absence of chemical denaturants, one can try to describe the change in protein Gibbs free energy as a function of the interatomic distances in the protein molecule which, in turn, are changed by variations in applied pressure. The use of pressure is also advantageous from a methodological point of view: the transition to native conditions (renaturation) is achieved simply by releasing the pressure and, in general, the effects of pressure on proteins are reversible and they are not accompanied by aggregation. The net volume change on denaturation comprises the effects of disruption of noncovalent bonds, changes in protein hydration, freeing of void volume and conformational changes. The reduction in the net volume seems to be largely the result of the disappearance of solvent-inaccessible voids inside the protein.

4.3.1. Equilibrium studies of protein unfolding. As an example, we present data on the pressure induced unfolding and refolding of Staphylococcal nuclease (Snase). These studies were performed using synchrotron small-angle x-ray scattering, which monitors changes in the tertiary structural properties of the protein upon pressurization or depressurization. Snase is a small protein of about 17.5 kDa containing 149 amino acids and no disulfide bonds. In the crystalline state, the protein contains 26.2% helices, 24.8% β-sheets (barrel), 7.4% extended chains, 24.8% turns and loops and 8.7% unordered chains (8.1% are uncertain). As an example of a SAXS curve taken under high pressure conditions, figure 11(a) exhibits the diffraction pattern of Snase at 1000 bar and 25 °C; figure 11(b) depicts the Guinier plot of native Snase at room temperature as obtained form the SAXS data. Analysis of the high pressure SAXS data reveals that over a pressure range from atmospheric pressure to approximately 3 kbar, the radius of gyration R_g of the protein increases from a value near 17 Å for native Snase twofold to a value near 35 Å (figure 12) [59, 60]. A large broadening of the pair-distance

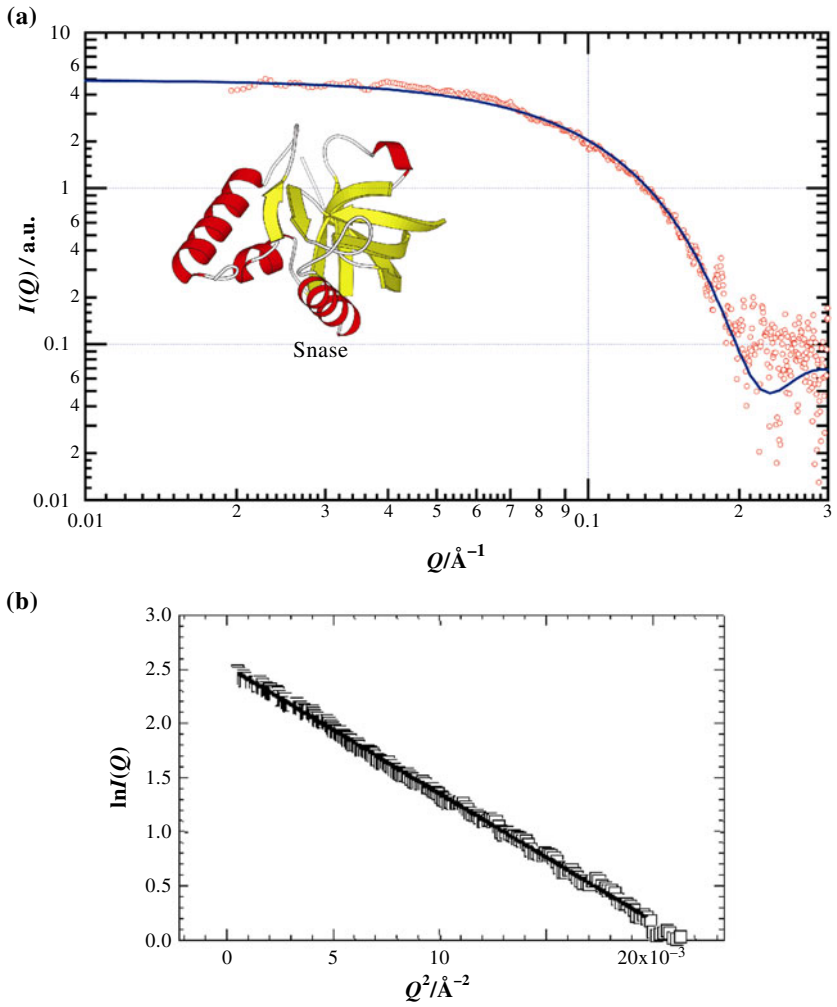

Figure 11. (a) Comparison of the SAXS curve of Snase (inset: native structure) calculated by CRYSOL with the experimental data (open points) at 1000 bar and 25 °C. CRYSOL uses the atomic coordinates stored in the file PDB Brookhaven data bank to calculate a three-dimensional envelope which is surrounded by a virtual shell of solvent molecules (thickness 3 Å). The solid curve represents the resulting scattering curve of the envelope including the solvent shell. The intensity $I(0)$ at $Q = 0$ and the background scattering intensity are the only parameters that have been varied. (b) A Guinier plot of the SAXS data of native Snase at room temperature. Using equation (19), a radius of gyration R_g of ∼17 Å is obtained.

distribution function $p(r)$ is observed over the same range, indicating a transition from a globular to a more ellipsoidal-like structure (figure 13). Complementary FT-IR measurements show that the pressure induced denatured state above 3 kbar retains nonetheless some degree of β-like secondary structure and the molecules cannot be described as a fully extended random polypeptide coil (no typical Kratky plot), which is in accord with the SAXS results. Assuming the pressure induced unfolding transition of Snase to occur essentially as a two-state process, analysis of the concentration–pressure profiles yields a Gibbs free energy change for unfolding of $\Delta G_u^\circ = 17 \pm 4$ kJ mol^{-1} and a volume change for unfolding of $\Delta V_u^\circ = -80 \pm 20$ ml mol^{-1}

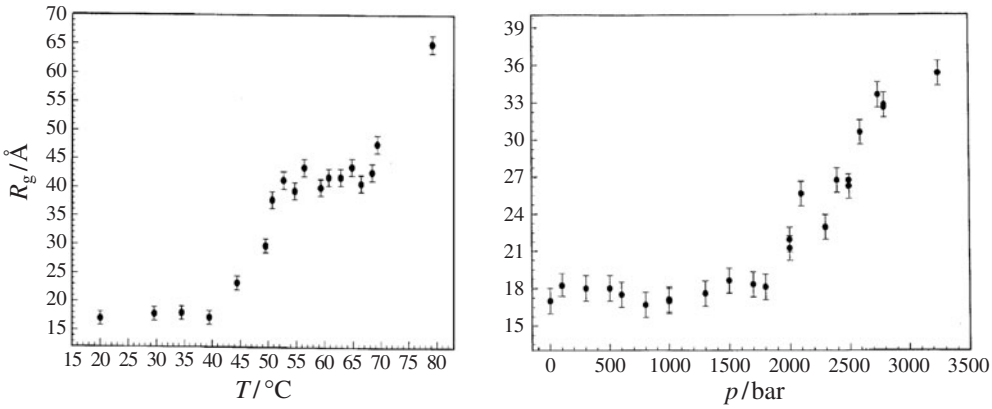

Figure 12. The radius of gyration R_g of Snase (1% (w/w), pH 5.5) as a function of temperature and pressure (at $T = 20\,^{\circ}\mathrm{C}$).

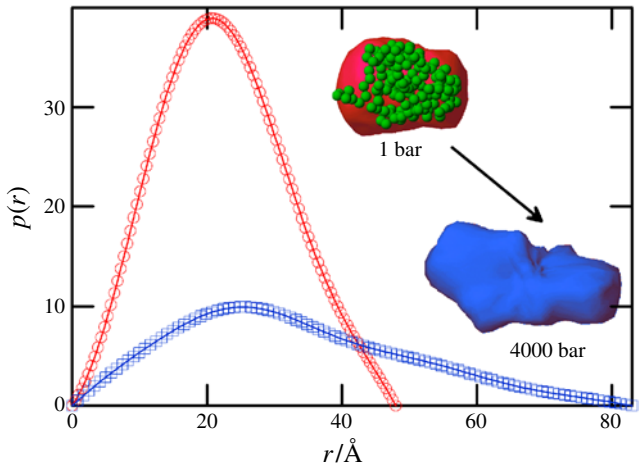

Figure 13. The pair-distance distribution function $p(r)$ of Snase (1% (w/w), pH 5.5) at two selected pressures, 1 and 4000 bar ($T = 25\,^{\circ}\mathrm{C}$). The size of the protein shape increases from about $46 \times 46 \times 49$ Å^3 to about $60 \times 60 \times 80$ Å^3. Within the envelope of the 1 bar structure, the shape of the crystal structure of native Snase is embedded.

at ambient temperature and pressure. For comparison, temperature induced denaturation involves a further unfolding of the protein molecule which is indicated by a larger R_g value of 45 Å (figure 12) and significantly lower fractional intensities of IR bands associated with secondary structure.

The pressure mid-points at several temperatures obtained from the FT-IR and SAXS profiles are plotted as a phase diagram in figure 14 [59, 60]. It exhibits the curvature which is typical of heat and cold denaturation of many monomeric proteins. The phase diagram will certainly depend on the individual protein secondary structural composition and will be more complicated for larger protein systems. Also additional regions in the phase diagram may appear, such as an extended region at high temperatures where aggregation occurs. One must also be aware of the fact that the unfolded states in the p–T plane can be of considerably different structure, and that long-lived metastable phases may occur.

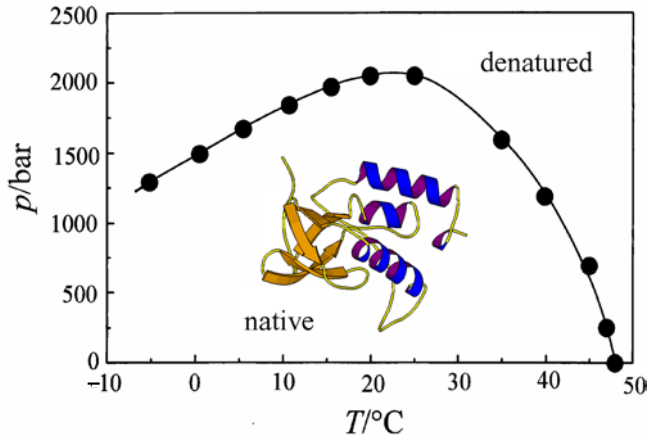

Figure 14. The T, p stability diagram of Snase at pH 5.5.

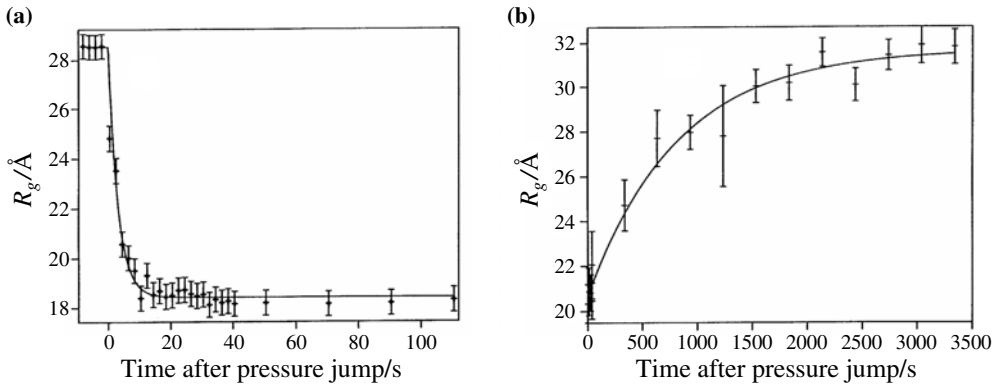

Figure 15. (a) Time evolution of the radius of gyration R_g of Snase (1% (w/w), pH 5.5) after a negative pressure jump from 4000 to 800 bar. The fit of data to a single-exponential decay function (curve) yields a time constant of 4.5 s. (b) The time dependence of the increase in R_g after a positive pressure jump from 1500 to 3000 bar. The fit of the data to a single-exponential function (curve) yields a time constant of 14 min.

4.3.2. Kinetic studies of the unfolding/refolding reaction of proteins. By crossing the phase boundary by applying a p jump, the folding and refolding kinetics can be studied [12, 60]. The more detailed analysis of the kinetic SAXS data starts with the determination of the radius of gyration, roughly with a Guinier plot and more accurately with the indirect Fourier transformation. As can be seen in figure 15, the rapid decrease of pressure for a solution of Snase at 25 °C from for example 4000 bar (denaturing conditions) to 800 bar (native conditions) results in a relatively rapid decrease in the value of the radius of gyration, R_g, from near 29 to 18 Å. The observed pressure jump relaxation profile for the decrease in R_g fits well to a single-exponential decay with a time constant τ of 4.5 s. In contrast, a positive pressure jump at 25 °C from 1500 bar (near-native conditions) to 3000 bar (fully denaturing conditions) results in a very slow relaxation of R_g from 20 to 31 Å. As for the negative pressure jumps, the positive pressure jump profile is well fitted by a single-exponential function, with a much longer time constant of $\tau = 14$ min.

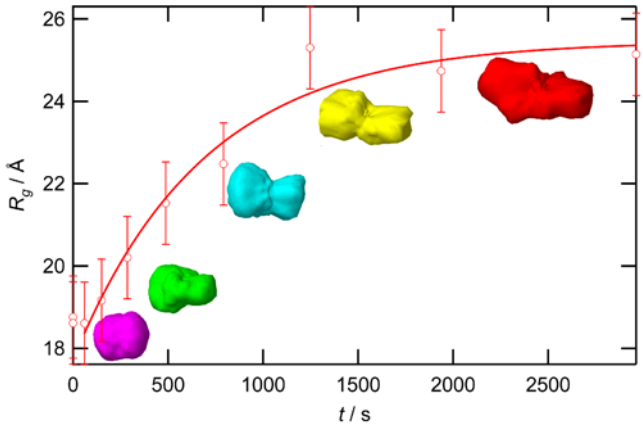

Figure 16. The time evolution of the radius of gyration R_g (including the solvation shell) of Snase (1% (w/w), pH 5.5) after a pressure jump from 1 to 3.5 kbar at $T = 25\,^{\circ}$C. The displayed shapes are calculated with the program DAMMIN assuming an initial spherical or oblate arrangement of 'dummy atoms'. Both assumptions lead to comparable shapes. All other parameters are taken from the GNOM output file (experimental data, fitted curve, error information, maximum radius of the pair-distance distribution).

Analysis of the SAXS data with the program package GNOM, CRYSOL, DAMMIN and viewing program MASSAH reveal a more detailed picture of structural changes during the folding/unfolding process [17, 25–28]. The program GNOM is used to calculate the pair-distance distribution function from the scattering data. The output data can be used to start an *ab initio* shape determination, which is done by the program DAMMIN and a three-dimensional shape model is generated. Figure 16 shows the time evolution of R_g for Snase after a pressure jump from 1000 to 3500 bar as obtained by GNOM. At 1000 bar, $R_g \approx 18.7$ Å (taking into account the hydration sphere now) which is comparable to the result obtained by CRYSOL ($R_g^{solv} = 19.4$ Å), which is based on the x-ray crystal structure for the native protein. Furthermore, the program DAMMIN is used to calculate shape models of the transitional and unfolded states. They represent an average over the complete ensemble and a time period of 10 ms (exposure time). DAMMIN begins the *ab initio* shape modelling with a spherical or oblate three-dimensional array of 'dummy atoms'. The maximum extension of the pair-distance distribution serves as a scale for the positions of the atoms. With these predictions a scattering curve can be calculated from this array. During the modelling process, the arrangement of the 'dummy atoms' is varied until the calculated curve fits the result of the previous GNOM calculations. Figure 16 also exhibits a series of shape models for Snase as function of time during unfolding. Unlike the case for the folded state, certainly no structural information with atomic resolution exists of the unfolded protein, which consists of an ensemble of different more or less disordered states.

We find from an analysis of the kinetic data shown in figures 15 and 16 that the activation volume for folding is large and positive (57 ± 4 mL mol^{-1}) and that for unfolding seems to be small and negative (-23 ± 3 mL mol^{-1}) [12, 60]. The volume of the protein–solvent system in the transition state is thus significantly larger than in the unfolded state and somewhat smaller than in the folded state, so the transition state lies closer to the folded than to the unfolded state in terms of system volumes. The positive activation volume for the folding process, which is responsible for the large increase in the relaxation time with pressure (allowing us to observe this process without resorting to ultrafast methods), implies dehydration in the rate limiting step for folding.

The stage is now well set for further work addressing more complex questions, such as the study of the folding reaction of oligomers and protein complex formation as well as for studies of aggregation phenomena. Pressure studies might also lead to a better understanding of the interactions that lead to aggregation and will thus enhance our ability to design inhibitors and therapeutics for aggregation driven diseases, such as Alzheimer's, Parkinson's and prion diseases. These examples clearly demonstrate that pressure dependent studies can help delineate the free energy landscape of proteins and hence help elucidate which features are essential in determining the uniqueness and stability of the native conformational state.

Acknowledgments

Financial support from the Deutsche Forschungsgemeinschaft (DFG) and the Fonds der Chemischen Industrie is gratefully acknowledged.

References

[1] Balny C, Hayashi R, Heremans K and Masson P (ed) 1992 *High Pressure and Biotechnology* (*Colloque Inserm* vol 224) (Montrouge: John Libbey Eurotext)
[2] Mozhaev V V, Heremans K, Frank H, Masson P and Balny C 1994 *Tibtech* **12** 493
[3] Ludwig H (ed) 1998 *Advances in High Pressure Bioscience and Biotechnology* (Berlin: Springer)
[4] Winter R and Jonas J (ed) 1999 *High Pressure Molecular Science* (*NATO ASI Series E358*) (Dordrecht: Kluwer-Academic)
[5] Winter R (ed) 2003 *High Pressure Bioscience and Biotechnology II* (Heidelberg: Springer)
[6] Winter R 2002 High pressure effects in molecular biophysics *Proc. Int. School of Physics 'Enrico Fermi', Course CXLVII on High Pressure Phenomena* ed R J Hemley, G L Chiarotti, M Bernasconi and L Ulivi (Amsterdam: IOS Press) p 413
[7] Kato C and Hayashi R 1999 *Biosci. Biotechnol. Biochem.* **63** 1321
[8] Abe F, Kato C and Horikoshi K 1999 *Trends Microbiol.* **7** 447
[9] Rostain J C, Martinez E and Lemaire C (ed) 1989 *High Pressure Nervous Syndrome—20 Years Later* (Amsterdam: ARAS-SNHP Publications)
[10] Gross M and Jaenicke R 1994 *Eur. J. Biochem.* **221** 617
[11] Mozhaev V V, Heremans K, Frank J, Masson P and Balny C 1996 *Struct. Funct. Genet.* **24** 81
[12] Woenckhaus J, Köhling R, Winter R, Thiyagarajan P and Finet S 2000 *Rev. Sci. Instrum.* **71** 3895
[13] Winter R and Czeslik C 2000 *Z. Kristallogr.* **215** 454
[14] Büldt G, Schlesinger R, Pebay-Peyrola E and Sass H J G 2000 Structure and dynamics of biological membranes *Structure and Dynamics of Biomolecules: Neutron and Synchrotron Radiation for Condensed Matter Studies* ed E Fanchon, E Geissler, J-L Hodeau, J-R Regnard and P A Timmins (Oxford: Oxford University Press) p 251
[15] Winter R, Erbes J, Czeslik C and Gabke A 1998 *J. Phys.: Condens. Matter* **10** 11499
[16] Laggner P 1988 *Springer Topics in Current Chemistry* vol 145 (Heidelberg: Springer) p 173
[17] Kratky O and Laggner P 1987 *Encyclopedia of Physical Science and Technology* vol 14 (New York: Academic) p 693
[18] Feigin L A and Svergun D I 1987 *Structure Analysis by Small Angle X-Ray and Neutron Scattering* (New York: Plenum)
[19] Glatter O and Kratky O 1982 *Small-Angle X-Ray Scattering* (New York: Academic)
[20] Guinier A and Fournet A 1995 *Small Angle Scattering of X-Rays* (New York: Wiley)
[21] Lindner P and Zemb T (ed) 1991 *Neutron, X-Ray and Light Scattering: Introduction to an Investigative Tool for Colloidal and Polymeric Systems* (Amsterdam: North-Holland)
[22] Kajiwara K and Hiragi Y 1996 Structure analysis by small-angle x-ray scattering *Applications of Synchrotron Radiation to Materials Analysis* ed H Saisho and Y Gohshi (Amsterdam: Elsevier) chapter 6, p 353
[23] Winter R and Noll F 1998 *Methoden der Biophysikalischen Chemie* (Stuttgart: Teubner)
[24] Baruchel J, Hodeau J L, Lehmann M S, Regnard J R and Schlenker C 1994 *Neutron and Synchrotron Radiation for Condensed Matter Studies* (*Hercules—Higher European Research Course for Users of Large Experimental Systems* vols 1–3) (Heidelberg: Springer)

[25] Vachette P and Svergun D 2000 Small-angle x-ray scattering by solutions of biological macromolecules *Structure and Dynamics of Biomolecules: Neutron and Synchrotron Radiation for Condensed Matter Studies* ed E Fanchon, E Geissler, J-L Hodeau, J-R Regnard and P A Timmins (Oxford: Oxford University Press) p 199
[26] Svergun D, Barberato C and Koch M H J 1995 *J. Appl. Crystallogr.* **28** 768
[27] Svergun D I 1999 *Biophys. J.* **79** 2879
[28] Petoukhov M V, Eady N A J, Brown K A and Svergun D I 2002 *Biophys. J.* **83** 3113
[29] Cevc G (ed) 1993 *Phospholipids Handbook* (New York: Dekker)
[30] Lipowski R and Sackmann E (ed) 1995 *Structure and Dynamics of Membranes* vols 1A, 1B (Amsterdam: Elsevier)
[31] Seddon J M 1990 *Biochim. Biophys. Acta* **1031** 1
[32] Tate M W, Eikenberry E F, Turner D C, Shyamsunder E and Gruner S M 1991 *Chem. Phys. Lipids* **57** 147
[33] Hyde S, Andersson S, Larsson K, Blum Z, Landh T, Lidin S and Ninham B W 1997 *The Language of Shape. The Role of Curvature in Condensed Matter: Physics, Chemistry and Biology* (Amsterdam: Elsevier)
[34] Böttner M, Ceh D, Jakobs U and Winter R 1994 *Z. Phys. Chem.* **184** 205
[35] Winter R and Pilgrim W C 1989 *Ber. Bunsenges. Phys. Chem.* **93** 708
[36] Czeslik C, Reis O, Winter R and Rapp G 1998 *Chem. Phys. Lipids* **91** 135
[37] Worcester D and Hammouda B 1998 *Physica* B **241–243** 1175
[38] Luzzati V 1997 *Curr. Opin. Struct. Biol.* **7** 661
[39] Landh T 1995 *FEBS Lett.* **369** 1
[40] Chung H and Caffrey M 1995 *Biophys. J.* **69** 1951
[41] Briggs J, Chung H and Caffrey M 1996 *J. Physique* II **6** 723
[42] Reis O and Winter R 1998 *Langmuir* **14** 2903
[43] Czeslik C, Winter R, Rapp G and Bartels K 1995 *Biophys. J.* **68** 1423
[44] Winter R, Gabke A, Czeslik C and Pfeifer P 1999 *Phys. Rev.* E **60** 7354
[45] Jørgensen K and Mouritsen O G 1995 *Biophys. J.* **95** 942
[46] Bernsdorff C and Winter R 1996 *Z. Phys. Chem.* **193** 151
[47] Zein M and Winter R 2000 *Phys. Chem. Chem. Phys.* **2** 4545
[48] Eisenblätter J and Winter R 2000 *Magn. Reson. Chem.* **38** 662
[49] Erbes J, Winter R and Rapp G 1996 *Ber. Bunsenges. Phys. Chem.* **100** 1713
[50] Erbes J, Gabke A, Rapp G and Winter R 2000 *Phys. Chem. Chem. Phys.* **2** 151
[51] Caffrey M, Hogan J and Mencke A 1991 *Biophys. J.* **60** 456
[52] Steinhart M, Kriechbaum M, Pressl K, Amenitsch H and Laggner P 1999 *Rev. Sci. Instrum.* **70** 1540
[53] Squires A, Templer R H, Ces O, Gabke A, Woenckhaus J, Seddon J M and Winter R 2000 *Langmuir* **16** 3578
[54] Squires A M, Templer R H, Seddon J M, Woenckhaus J and Winter R 2002 *Langmuir* **18** 7384
[55] Seddon J M, Squires A, Ces O, Templer R H, Woenckhaus J and Winter R 2003 *Self Assembly—the Future* ed B H Robinson (Amsterdam: IOS Press) at press
[56] Heremans K and Smeller L 1998 *Biochim. Biophys. Acta* **1386** 353
[57] Mozhaev V V, Bec N and Balny C 1994 *Biochem. Mol. Biol. Int.* **34** 191
[58] Jonas J, Ballard L and Nash D 1998 *Biophys. J.* **75** 445
[59] Panick G, Malessa R, Winter R, Rapp G, Frye K J and Royer C 1998 *J. Mol. Biol.* **275** 389
[60] Panick G, Vidugiris C J A, Malessa R, Rapp G, Winter R and Royer C 1999 *Biochemistry* **38** 4157